




## Cohesive Sediment Erosion in a Combined Wave-Current Boundary Layer

Galen Egan<sup>1</sup> , Grace Chang<sup>2</sup> , Samuel McWilliams<sup>2</sup>, Gene Revelas<sup>3</sup>, Oliver Fringer<sup>1</sup>, and Stephen Monismith<sup>1</sup> 

<sup>1</sup>Department of Civil and Environmental Engineering, Stanford University, Stanford, CA, USA, <sup>2</sup>Integral Consulting Inc., Santa Cruz, CA, USA, <sup>3</sup>Integral Consulting Inc., Olympia, WA, USA

### Key Points:

- Wave shear stress drives erosion by mobilizing sediment in the wave bottom boundary layer
- Tidal turbulence in the absence of waves is poorly correlated to erosion
- Boundary layer sediment fluxes are consistent with bed level measurements, laboratory flume studies, and previous field work

### Correspondence to:

G. Egan,  
[gegan@stanford.edu](mailto:gegan@stanford.edu)

### Citation:

Egan, G., Chang, G., McWilliams, S., Revelas, G., Fringer, O., & Monismith, S. (2021). Cohesive sediment erosion in a combined wave-current boundary layer. *Journal of Geophysical Research: Oceans*, 126, e2020JC016655. <https://doi.org/10.1029/2020JC016655>

Received 28 JUL 2020  
Accepted 16 DEC 2020

**Abstract** We conducted field work on the shoals of South San Francisco Bay to elucidate the mechanisms driving cohesive sediment erosion in a shallow, wave- and current-driven flow. Compiling data from three deployments, including measurements taken within the combined wave-current boundary layer, we found that wave shear stress was strongly correlated to turbulent sediment fluxes across all seasons and a range of deployment depths. Tidal turbulence was only correlated to turbulent sediment fluxes for larger relative depths, or when a wave-driven sediment flux in the bottom boundary layer allowed the tidal shear stress to transport sediment into the overlying flow. Despite the dominance of waves in eroding sediment, we found favorable agreement between *in situ* boundary layer erosion measurements and laboratory erosion measurements conducted in a steady flume. Results were analyzed in the context of two benthic surveys which provided insight into the sediment bed properties.

**Plain Language Summary** Marine sediments cover the majority of the Earth's surface, and the movement of sediment through the environment affects water quality, coastal infrastructure, and the health of aquatic ecosystems. Sediments are primarily transported due to a combination of forces exerted by wave and tidally driven flows. However, the erosion (or picking up) of sediment from the sea floor by the flow is a complex process that occurs over very small spatial scales. Therefore, it is difficult to observe and is not particularly well-understood. In this paper, we use new measurement devices to observe how mud erodes in an estuary with varying wave and tidal conditions. We found that waves can effectively erode sediment into a thin region near the bed, allowing tidal currents to distribute the sediment throughout the rest of the water column. We compared these field erosion measurements with various other traditional measurement techniques and previous studies, and found general agreement among them. These results can be applied to improving computer models of sediment transport.

## 1. Introduction

Sediment erosion is a ubiquitous geophysical phenomenon that affects habitat restoration efforts, contaminated sediment remediation, and navigational dredging (Van Maren et al., 2015; Wood & Armitage, 1997). These processes are often simulated in numerical sediment transport models. While coarse-grained sediments (e.g., quartz) can be treated as single particles to determine model parameters such as critical shear stress for erosion, estuarine sediments, which contain large percentages of minerals such as silt and clay, can aggregate together to form suspended flocs and a continuum bed (Winterwerp & Van Kesteren, 2004). The characteristics of flocs make their erosion from the bed and subsequent vertical distribution in the water column difficult to predict. Therefore, many models rely on empirical parameterizations rather than first principles (Merritt et al., 2003; Papanicolaou et al., 2008).

Model parameterizations are often informed by field observations, which generally focus on the interplay between cohesive sediment dynamics and local hydrodynamics. In South San Francisco Bay, California, USA, the flow is driven by both tidal currents and short-period wind waves. This combination leads to non-linear interactions between the wave and tidally driven turbulence near the bottom boundary. Numerous analytical models have been proposed to describe these dynamics (Christoffersen & Jonsson, 1985; Coffey & Nielsen, 1987; W. Grant & Madsen, 1979; You et al., 1991), and characteristics of the combined wave-current shear stress were analyzed for our study site in Egan et al. (2019). Connecting the hydrodynamics to erosion, field observations have shown that wave and current interactions significantly enhance sediment

resuspension (Brand et al., 2010; Friedrichs et al., 2000; MacVean & Lacy, 2014). When waves erode sediment into the wave boundary layer, the mean current can more readily entrain sediment higher in the water column (Friedrichs et al., 2000).

Erosion has been studied in the laboratory as well. Flume studies have shown that the critical shear stress of the sediment bed increases with depth into the bed and the amount of time the bed consolidates (Mehta & Partheniades, 1982). These studies produced a semi-empirical erosion formula that varied exponentially with the normalized excess shear stress (i.e., excess applied stress relative to critical shear stress). Aside from exponential formulations, researchers have put forth power law (Lick, 1982; Maa et al., 1998) and linear erosion relationships (Mei et al., 1997; Sanford & Halka, 1993). One of the most widely used models is a unified erosion formulation validated on field measurements that describes both Type I erosion (depth-limited, i.e., shear forcing cannot keep up with increases in bed shear strength as erosion progresses) and Type II erosion (unlimited, i.e., erosion continues unimpeded because the shear forcing remains stronger than bed shear strength) (Sanford & Maa, 2001). More complex models accounting for transient armoring, consolidation, and bioturbation have also been proposed (Sanford, 2008).

Due to the small spatial scales over which erosion occurs, it has historically been difficult to observe and quantify its driving mechanisms *in situ*. This has resulted in a relatively low-resolution understanding of a process that occurs over turbulent timescales in the millimeter-scale bottom boundary layer. Leveraging novel acoustic instrumentation, we simultaneously measured shear stress, sediment fluxes, and bed level within the combined wave-current boundary layer to elucidate the competing roles of waves and currents in eroding sediment from a muddy bed in South San Francisco Bay. This resulted in, to our knowledge, the first direct field measurements of a sediment flux coherent with the wave motion in an estuarine wave boundary layer. With data taken from three separate month-long deployments, we also analyzed seasonal variability in the erosive response to hydrodynamic forcing. We compared these results to more traditional flume-based laboratory methods of measuring erosion, and comment on the applicability of these results to erosion parameterizations in sediment transport models.

## 2. Methods

### 2.1. Field Deployment

We deployed five instrument platforms on the shallow, eastern shoals of South San Francisco Bay for three 4-week periods: July 17, 2018–August 15, 2018 (summer deployment), January 10, 2019–February 7, 2019 (winter deployment), and April 17, 2019–May 15, 2019 (spring deployment). Study sites covered a range of mean water depths (Table 1) and the deployment dates were selected to sample a diverse set of estuarine conditions in terms of wave strength and phytoplankton productivity. Platform 1 (P1) held three acoustic Doppler velocimeters (ADVs) to measure turbulence and sediment fluxes throughout the water column, one profiling acoustic Doppler velocimeter (Vectrino) to measure turbulence and sediment fluxes in the bottom boundary layer, one acoustic Doppler current profiler (ADCP) to measure current profiles, and one RBR Bottom Pressure Recorder (BPR) to measure wave statistics. Approximately 30 meters from P1, we deployed an optical instrumentation platform (P1O) that contained two Sequoia Scientific Inc. LISST-100x's (LISST; Laser In-Situ Scattering and Transmissometry), which measured suspended sediment particle size distributions (PSDs). On platform 2 (P2) we deployed two ADVs, a LISST, and a BPR. Platform 3 (P3) held an additional ADV, ADCP, BPR, and three optical backscatter sensors (OBS). During the summer campaign, we deployed platform 4a (P4a) which contained the same instrumentation as P3. For the winter and spring deployments, we moved this platform south to better capture wave propagation and the tidal pressure gradient, and renamed it platform 4b (P4b). Platform locations are shown in Figure 1, and instrumentation details and study site information are summarized in Table 1, which includes platform GPS coordinates, mean lower-low water level (MLLW), and instrument deployment height in centimeters above the bed (cmab).

All ADVs were programmed to sample at 8 Hz for 14 min each hour, logging the pressure and 3D velocity. Each ADCP reported mean current profiles every 3 min based on 72 s of averaging. The BPRs logged pressure at 6 Hz for the entire deployment period, and each OBS reported turbidity every 5 min. The LISST at P1O collected a 60 s burst-averaged PSD every hour during the middle of the ADV sampling period, and the LISST at P2 measured a PSD every minute. The Vectrino was deployed with its measurement volume

Label	Location	MLLW (m)	Instrument	cmab
P1	37.58745°N, 122.18530°W	1.5	Vectrino Profiler	0–1.5
			ADV	5, 15, 45
			ADCP	15–400
			BPR	100
P1O	37.58730°N, 22.18530°W	1.5	LISST	15, 45
P2	37.58728°N, 122.17167°W	0.5	ADV	5, 15
			BPR	66
			LISST	35
P3	37.58550°N, 122.23141°W	2.5	ADV	15
			ADCP	15–400
			BPR	99
			OBS	15, 30, 80
P4a	37.58681°N, 122.21182°W	2.25	Same as P3	
P4b	37.56130°N, 122.18530°W	2.25	Same as P3	

overlapping the bed such that it reported the 3D velocity at 64 Hz with 1 mm vertical resolution from 0 to 1.5 cmab for 12 min each hour in the summer, and 14 min each hour in the spring. Each of those deployments resulted in approximately two weeks of usable Vectrino data; after that point the measurement volume was either located too close to, or too far from the bed. The Vectrino collected no data during the winter because of a battery failure. Additional details about the deployment can be found in our previous paper analyzing the wave-current boundary layer dynamics at P1 (Egan et al., 2019).

In addition to deploying moored platforms, we collected two sediment box cores from each study site one day prior to the summer deployment. These cores were placed in a US Environmental Protection Agency and Army Corps of Engineers certified Sediment Erosion with Depth flume (SEDflume) to characterize erosion rates and critical shear stress with depth into the core (McNeil et al., 1996; Roberts et al., 1998). The sediment bulk density was also measured at each erosion depth interval.

During the winter and spring deployments, we conducted a sediment bed survey adjacent to P1 using an Ocean Imaging Systems Sediment Profile Imaging (SPI) camera (Rhoads & Germano, 1982; Rhoads & Germano, 1987). The SPI survey allowed for characterization of sediment bed properties at the sediment-water interface and 10–20 cm into the bed, along with biological activity through visual identification of sediment grain size, feeding voids, worm tubes, and burrows. Erosion data were analyzed in the context of these sediment bed characteristics.

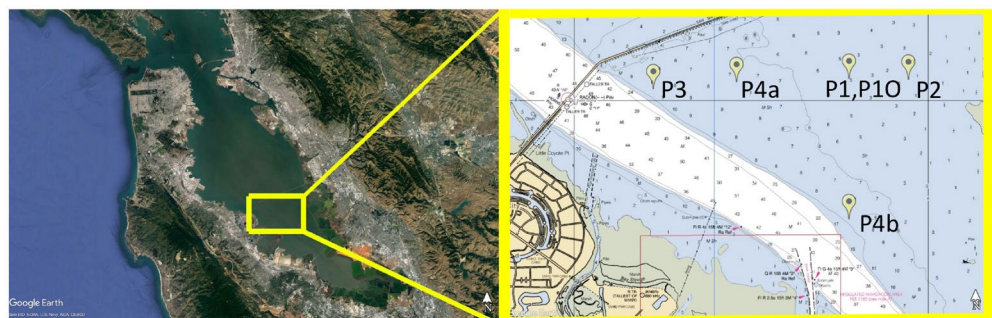


**Figure 1.** Study sites in South San Francisco Bay. P1, P1O, P2, and P3 were deployed in the summer, winter, and spring; P4a was only deployed in the summer, and was replaced by P4b in the winter and spring.

## 2.2. SEDflume and SPI

Two SEDflume cores were collected from sites P1, P2, and P3 one day prior to the summer deployment. Core depths ranged from 31–52 cm, and each core had a cross-sectional area of  $10 \times 15 \text{ cm}^2$ . Cores were eroded with progressively increasing shear stresses of 0.1, 0.2, 0.3, 0.4, 0.6, 0.8, 1.2, 1.6, 3.2, and 6.4 Pa. The shear stress was increased to the next increment after either 10 min had passed, or 1 cm of sediment had eroded. The shear stress sequence was repeated for three 4-cm vertical sections into the core. In each section, the erosion data were fit to the power law formula

$$E = E_0 \tau^b, \quad (1)$$

where  $E_0$  and  $b$  are empirical constants, and  $\tau$  is the shear stress. The critical shear stress,  $\tau_{cr}$ , was estimated as the shear stress corresponding to 0.5 mm of erosion in 10 min, that is, the minimum detectable amount of erosion during a shear stress increment. Because we are focusing our analysis on near-bed erosion, we will only report critical shear stresses and erosion rates for the first of the three 4-cm eroded sections, which is most relevant for comparison to our field data.

SPI surveys were conducted during the winter and spring deployments on January 9, 2019 and again on May 7, 2019, in the area surrounding P1. A total of 11 locations were sampled in January and 19 were sampled in May, with two duplicate images collected at each location. The SPI system consists of a Nikon D7100 digital single-lens reflex camera with a 24.1-megapixel image sensor mounted inside an Ocean Imaging Model 3731 pressure housing system. The images are taken through a prism which penetrates up to 20 cm into the sediment bed, with each image resulting in a  $14.5 \times 21 \text{ cm}^2$  profile view of the sediment-water interface. Camera settings were f10, ISO 400, and 1/60 shutter speed.

Image analysis was conducted using Integral Consulting Inc.'s MATLAB-based software, iSPI v1.1. The SPI image measured penetration depth, apparent redox potential discontinuity (aRPD) depth, grain size (in phi units), number of worm tubes on the surface, number of worm tubes at depth, number of feeding voids, burrows, and infaunal successional stage (Revelas et al., 2018). These parameters offered insight into the extent of biological activity at the bed and the vertical structure of bed properties, specifically in contrasting the relatively unconsolidated fluff layer at the bed with the firmer, more consolidated mud below.

## 2.3. Hydrodynamics

In South San Francisco Bay, the principal axis of the tidal ellipse runs approximately northwest to southeast, corresponding to the along-channel direction in Figure 1. Therefore, we rotated all ADV and Vectrino data into the coordinate system defined by the principal axes (i.e., the directions of maximum variance), as estimated by the ADCP mean velocity data at each of the platforms. The major component of velocity is denoted  $u$ , the minor component  $v$ , and the vertical velocity  $w$ . The flow was both wave- and current-driven, so each velocity component can be decomposed as

$$u = \bar{u} + \tilde{u} + u', \quad (2)$$

where  $\bar{u}$  is the velocity time averaged over a measurement burst period,  $\tilde{u}$  is the wave velocity, and  $u'$  is the turbulent fluctuating velocity.

Because the goal of this study was to examine the competing and synergistic roles of waves and currents in eroding sediment, it was necessary to define shear stresses that quantify the separate contributions of (a) currents, (b) waves, and (c) the combined action of the two. Such a decomposition can be achieved using the Grant-Madsen (GM) model (W. Grant & Madsen, 1979), which requires as input the bottom wave-orbital velocity,  $u_b$ , the mean velocity  $\bar{u}$ , at a reference height  $z = z_r$ , the wave frequency  $\omega$ , the angle between the waves and current  $\phi_{wec}$ , and the physical (or Nikuradse) bottom roughness,  $k_b$ . Each of these variables can be estimated from our data.

The mean velocity  $\bar{u}$ , was calculated from ADV data as the time-averaged velocity in the principal current direction at a height of  $z_r = 15 \text{ cm}$ . The bottom wave-orbital velocity was calculated following Wiberg and Sherwood (2008) as

$$u_b = \sqrt{2\text{var}(u')}, \quad (3)$$

again using 15 cmab ADV data. The magnitude of  $u_b$ , however, depends on the wave direction, which was not aligned with the major component of the tidal velocity. Therefore, we calculated  $u_b$  based on the fluctuating velocity in the dominant wave direction during each burst period, which was estimated using the methods described by Herbers et al. (1999). Similarly,  $\phi_{wc}$  was calculated as the difference between the dominant wave direction and the current direction (i.e., the direction of  $\bar{u}_r$ ). The wave frequency,  $\omega$ , was estimated from the peak in the power spectral density of the BPR pressure signal during 14 min segments corresponding to each ADV burst period. The power spectral density was calculated via the Welch method (Welch, 1967). The wave frequency was also used to estimate the wavenumber,  $k$ , using the linear gravity wave dispersion relation,  $\omega^2 = gk \tanh(kh)$ , where  $g$  is acceleration due to gravity and  $h$  is the mean water depth. Though the wavenumber is not required for the GM model, we will evaluate erosion trends across a range of relative depth ( $kh$ ) regimes in Section 3.4.

The final input to GM is the physical bottom roughness,  $k_b$ , which can be related to the bottom roughness,  $z_0$ , as  $k_b = 30z_0$ . To estimate  $z_0$ , we first calculated a drag coefficient,  $C_D$ . This was approximated as the best-fit slope from a least squares regression between the sign-preserving squared mean velocity at 15 cmab,  $u|u|$ , and the turbulent Reynolds stress at 15 cmab,  $-u'w'$ . The Reynolds stress was calculated using a spectral wave-turbulence decomposition (Bricker & Monismith, 2007). Because waves can increase the apparent bottom drag felt by the mean flow, we restricted the  $C_D$  regression to measurement burst periods where  $u_b < 0.05 \text{ m s}^{-1}$ . This ensured that wave activity did not erroneously skew the drag coefficient estimates, while retaining enough measurements for a reliable regression. Assuming a logarithmic velocity profile, the bottom roughness can be estimated in terms of  $C_D$  as

$$z_0 = \frac{z_r}{\exp\left(\frac{\kappa}{\sqrt{C_D}}\right)}, \quad (4)$$

where  $z_r = 15 \text{ cmab}$  is the reference height and  $\kappa = 0.41$  is the von Kármán constant. After calculating input variables at each platform during each season, the GM model produces estimates for the current-induced friction velocity,  $u_{*c}$ , the maximum wave friction velocity,  $u_{*wm}$ , and the combined wave-current friction velocity,  $u_{*wc}$ . Each of these can be cast in terms of a shear stress for the current, wave, and combined wave-current flow respectively,

$$\tau_c = \rho_0 u_{*c}^2 \quad (5a)$$

$$\tau_w = \rho_0 u_{*wm}^2 \quad (5b)$$

$$\tau_{wc} = \rho_0 u_{*wc}^2, \quad (5c)$$

where  $\rho_0$  is the fluid density. By analyzing the erosive response to each of the above shear stress estimates, we can elucidate the dominant physical mechanisms that drive cohesive sediment erosion in combined wave-current flows.

#### 2.4. Sediment

Sediment data, including multiple metrics for erosion, were primarily derived from acoustic instruments. This was preferable to using raw optical measurements because the acoustic instruments provided co-located measurements of shear stress to which erosion must be related. Acoustic backscatter readings from the Vecrino and P1 ADVs were calibrated against water samples with known suspended sediment concentration (SSC) in the lab, using sediment collected from the study site. The calibration curves can be found in Egan, Manning, et al. (2020). This method of SSC estimation has proven reliable for tracking relative changes in SSC over time at a single instrument (Brennan et al., 2002; Cartwright et al., 2013), though



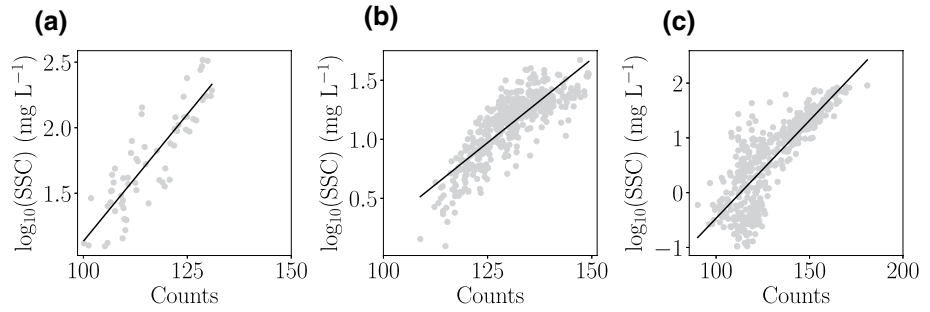


**Figure 2.** Acoustic backscatter (in instrument units of counts) to SSC calibration for 15 cmab ADVs at (a) Platform 2 ( $r^2 = 0.75$ ), (b) Platform 3 ( $r^2 = 0.69$ ), and (c) Platforms 4a and 4b ( $r^2 = 0.67$ ), with the black line indicating a least squares fit. ADVs, acoustic Doppler velocimeters; SSC, suspended sediment concentration.

the precise SSC magnitude should be interpreted with caution because variations in acoustic transmit frequency and suspended sediment particle size can affect the acoustic backscatter amplitude used to infer SSC (Lohrmann, 2001). The P2 ADV acoustic backscatter data were calibrated against in situ LISST SSC measurements, which were derived by summing the LISST PSDs and multiplying by the sediment density measured in the lab. OBS turbidity data were calibrated against SSC samples in the lab (not shown), allowing for calibration of the P3 and P4a/b ADVs against in situ OBS SSC data. These calibration curves are shown in Figure 2.

In addition to providing the mean SSC, these data were used to estimate the turbulent sediment flux,  $\overline{c'w'}$ , which was calculated as the covariance between SSC and the vertical velocity for both the Vectrino and ADV data. For the Vectrino, this resulted in a profile of  $\overline{c'w'}$ . We chose to vertically average this profile between 0.3 and 0.7 cmab for a near-bed estimate; this will be the reported Vectrino turbulent sediment flux value for the remainder of the paper.

Previous work in South San Francisco Bay used the turbulent sediment flux as a proxy for erosion (Brand et al., 2010), and we will do the same with a slight modification. Because we measured the sediment bulk density at each study site, we can normalize the turbulent sediment flux by the sediment density,  $\rho_s$ , to obtain an erosion estimate

$$E = \frac{\overline{c'w'}}{\rho_s}. \quad (6)$$

This is advantageous because it gives erosion in units of  $\text{m s}^{-1}$ , allowing for direct comparison with SED-flume results after fitting to the power law erosion formula (Equation 1). For the 5 cmab ADV and Vectrino  $E$  measurements, we can additionally estimate a critical shear stress by the same metric used for the SED-flume data, that is, finding the shear stress corresponding to 0.5 mm of erosion in 10 min, or  $8.33 \times 10^{-5} \text{ cm s}^{-1}$ . One implicit assumption during this fitting procedure is that  $\overline{c'w'}$  varies solely with the local shear stress. This is not strictly true; horizontal divergence in the sediment flux caused by, for example, tidal fronts or interactions with bedforms can affect  $\overline{c'w'}$  too. However, our sediment flux measurements (which were primarily near the bed) showed no clear tidal trends, and based on our SPI results (Section 3.1) and the small-grained sediments at our study sites, we do not expect significant effects from bedforms. Therefore, we will assume throughout the manuscript that the sediment flux is dominated by vertical processes.

We can measure erosion another way using the Vectrino bottom check feature. During each burst period, the Vectrino measured its distance from the nearest boundary. This was primarily used to calculate the vertical coordinates for velocity and SSC profiles, but bottom distance (BD) measurements can also be used to infer erosion rates. To that end, a fluctuating bed level,  $z_b$ , can be defined as

$$z_b = \overline{BD} - BD, \quad (7)$$

where  $\overline{BD}$  denotes the time-averaged bottom distance. This metric can be used as a proxy for erosion under the assumption that changes in  $z_b$  between bursts are due to sediment eroding or depositing beneath the

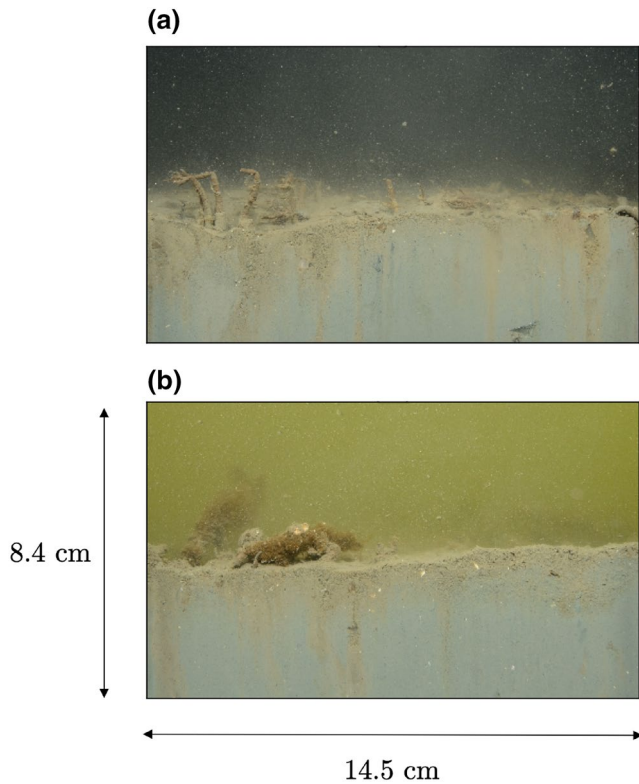


**Figure 3.** SPI camera images from the (a) winter survey and (b) spring survey. The dimensions of each image are 8.4 cm × 14.5 cm. SPI, sediment profile imaging.

May, were significantly shallower during the spring compared to the winter. The aRPD depth reflects the interplay between near-surface bioturbation rates and labile organic matter inputs. This temporal trend may point to increased organic inputs to the sediment bed and higher sediment oxygen demand in the spring. In half of the May images, brownish/red algae was evident on the sediment surface (Figure 3b); this was not evident in January. Higher water temperatures and nutrient concentrations, along with higher microbial activity and levels of ambient light would contribute to this algal growth. Alternatively, or as a contributing factor, the seasonal difference in aRPD depths could reflect recent scouring of the sediment surface and the erosion of well-mixed, aerobic, unconsolidated surface sediments.

**Table 2**

Summary Statistics From the Winter and Spring SPI Surveys

	Penetration depth (cm)	aRPD depth (cm)	Surface tube count	Feeding void count	Burrow count
Winter survey					
Avg	<b>13.0</b>	<b>3.2</b>	10	3	1
Min	8.8	1.5	1	1	0
Max	18.3	5.2	30	6	5
Spring survey					
Avg	<b>10.0</b>	<b>1.1</b>	9	3	1
Min	6.9	0.8	0	0	0
Max	11.3	1.5	20	5	3

Note: Bolded averaged are significantly different between surveys (Kolmogorov-Smirnov test,  $p < 0.05$ ).

instrument. That assumption may not always hold; for example,  $z_b$  could remain constant during erosive periods if the sediment under the Vectrino erodes at the same rate that the platform sinks into the bed. Platform consolidation is only expected to be significant immediately after deployment, however. Increases in  $z_b$  could also arise from transient clumps of sediment, flora, or fauna beneath the instrument, rather than from uniform deposition. These transient changes could be a substantial confounding factor, and will be considered when interpreting  $z_b$  data.

### 3. Results and Discussion

#### 3.1. SPI Survey and Bottom Roughness

Across both the winter and spring surveys, the SPI data indicated that the survey area was fine grained ( $>4$  phi major mode) with both surface tube-dwellers and subsurface deposit feeders present. Both large polychaete and amphipod (likely *ampelisca*) tubes were seen at the sediment surface in a number of the images (e.g., Figure 3a). Evidence of stage 3 infauna (i.e., subsurface feeding voids, worms, or burrows) was observed in all but one of the images. Overall, the area surveyed in both the winter and spring appeared to be a relatively undisturbed, soft-bottom benthic habitat with a diverse benthic infaunal assemblage.

Table 2 shows the summary statistics for five of the parameters measured from the images (penetration and aRPD depths, and counts for surface tubes, feeding voids, and burrows) for the winter and spring data separately. Two-sample Kolmogorov-Smirnov tests were run to determine which of the six parameters were significantly different between surveys at a 5% significance level.

Both penetration depth, which averaged 13 cm in January and 10 cm in May, and aRPD depth, which averaged 3.2 cm in January and 1.1 cm in May, were significantly shallower during the spring compared to the winter. The aRPD depth reflects the interplay between near-surface bioturbation rates and labile organic matter inputs. This temporal trend may point to increased organic inputs to the sediment bed and higher sediment oxygen demand in the spring. In half of the May images, brownish/red algae was evident on the sediment surface (Figure 3b); this was not evident in January. Higher water temperatures and nutrient concentrations, along with higher microbial activity and levels of ambient light would contribute to this algal growth. Alternatively, or as a contributing factor, the seasonal difference in aRPD depths could reflect recent scouring of the sediment surface and the erosion of well-mixed, aerobic, unconsolidated surface sediments.

The reduced penetration depths in the spring suggest a firmer substrate in May than in January. This could reflect less intensive biogenic sediment mixing in the spring. However, there does not appear to be a major shift in community structure based on the lack of significant differences between the counts of the infauna themselves and their biogenic structures between January and May. Alternative explanations for the reduced prism penetration in May is the surface algal debris providing resistance to prism's descent into the sediment column and/or the recent erosion of the surface well-mixed layer, leaving more consolidated sediments in place. If the latter explanation is to blame for the reduced penetration depths, the spring erosion rates may be significantly reduced relative to winter given a constant bed shear stress. This potential change in bed composition will be revisited in the following sections as we analyze erosion data in the context of the SPI results.

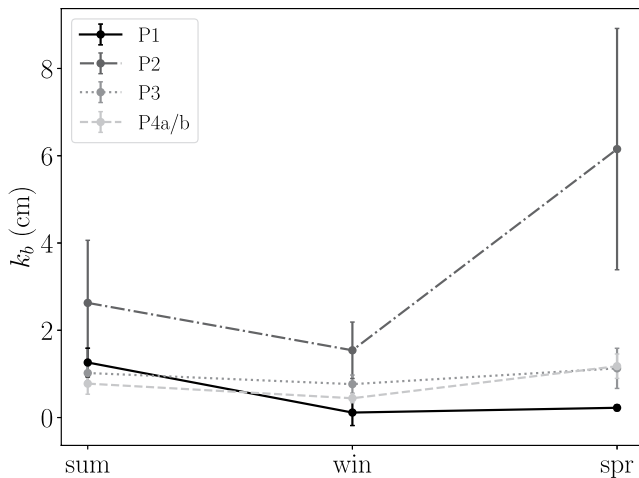


**Figure 4.** The physical bottom roughness,  $k_b$ , calculated via Equation 4 for each study site during each deployment from 15 cmab ADV data. ADV, acoustic Doppler velocimeter.

While the SPI survey focused on benthic conditions at P1, the time-varying nature of the sediment bed at the other study sites can be examined through bottom roughness calculations. Figure 4 shows the physical bottom roughness,  $k_b$ , at each of our platforms for the summer, winter, and spring deployments. At P1, the bed was significantly rougher during the summer. This trend is discussed in detail in a previous paper (Egan, Chang, et al., 2020), and is due to the increased density of benthic feeding tubes during the summer relative to the winter and spring. P3 and P4a/b show similar trends to each other, with a slight reduction in  $k_b$  from summer to winter, and a more substantial increase from winter to spring. Across all deployments, roughness was largest at P2, especially in the spring. During SEDflume core collection, we noted an abundance of clam shells on the sediment bed at P2, which likely caused the enhanced roughness relative to the other platforms.

The results in Figure 4 emphasize that bed conditions can change dramatically in both time and space, with  $k_b$  values ranging from a low of 0.11 cm to a high of 6.15 cm. The bottom roughness is a key parameter in the GM model, and sweeping its input value over more than an order of magnitude would produce widely varying bed shear stress estimates.

Excluding the anomalously high spring P2 value, the average bottom roughness across all deployments and study sites was 1.1 cm. Therefore, an input of  $k_b \approx 1$  cm may be broadly appropriate for this region, and absent any highly localized measurements it would be difficult to recommend a more accurate value.

### 3.2. Boundary Layer Sediment Flux Measurements

We can gain significant insight into the erosion dynamics at P1 by examining the near-bed response surrounding a large wind event. Plotted in Figures 5a–5c are the bottom wave-orbital velocity, the near-bed erosive flux magnitude, and the bottom distance, respectively, for seven days of the spring deployment. Strong winds on 04/20 led to the largest bottom wave-orbital velocities that we measured during any of the deployments (Figure 5a), which were correlated to elevated sediment flux magnitudes (Figure 5b).

While the correlation between wave strength and turbulent sediment flux is not surprising, the unique aspect of this data set is the simultaneous measurement of bed level (Figure 5c). As the wave strength

and sediment flux increased on 04/19, the bed level decreased, a direct measurement of erosion. Just before 04/20 00:00,  $z_b$  again increased, which may indicate deposition during the weak wave period. On 04/20,  $u_b$  and  $|E|$  increase throughout the day, leading to 1.02 cm of erosion in terms of  $z_b$  from midnight 04/19 to midnight 04/20. This corresponds to an erosion rate of  $1.18 \times 10^{-5} \text{ cm s}^{-1}$ . As a comparison, Figure 5b gives  $|E| = 1.36 \times 10^{-5} \text{ cm s}^{-1}$  averaged over the same period. These data are remarkably well-correlated, lending confidence to the SSC calibration of the Vecrino acoustic backscatter. The agreement also helps justify the assumption that the turbulent sediment flux is primarily influenced by 1D vertical processes and is a reliable proxy for erosion from the bed.

Once the strong winds subsided on 04/21, there were rapid fluctuations in  $z_b$ ; these could be due to either enhanced deposition after the storm or transient benthic flora/fauna beneath the Vecrino. Afterward, there was a relative decrease in mean bed level compared to the prestorm period, from approximately 0.3 cm to  $-0.1$  cm. This could indicate permanent erosion of part of the unconsolidated fluff layer seen in the SPI image (Figure 3b). The poststorm  $z_b$  signal also showed fundamentally different behavior with wave strength (Figure 6). For the three days prior to the storm,  $z_b$  decreased with wave shear stress as expected. Afterwards,  $z_b$  was

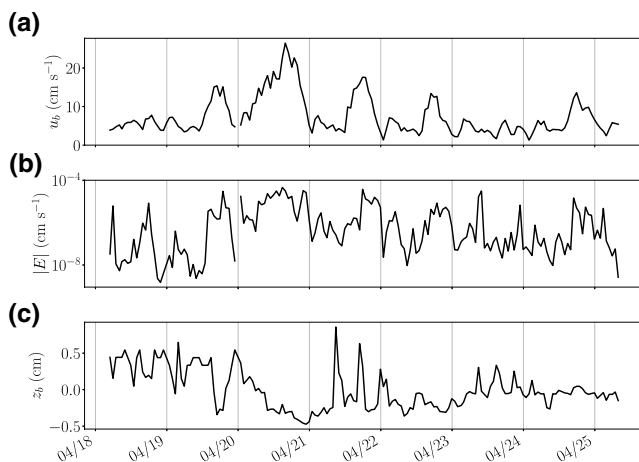


**Figure 5.** Seven day time series during the spring deployment showing Vecrino measurements of (a) the bottom wave-orbital velocity,  $u_b$ , (b) the erosive sediment flux magnitude,  $|E|$  (Equation 6), and (c) the fluctuating bed level,  $z_b$  (Equation 7).



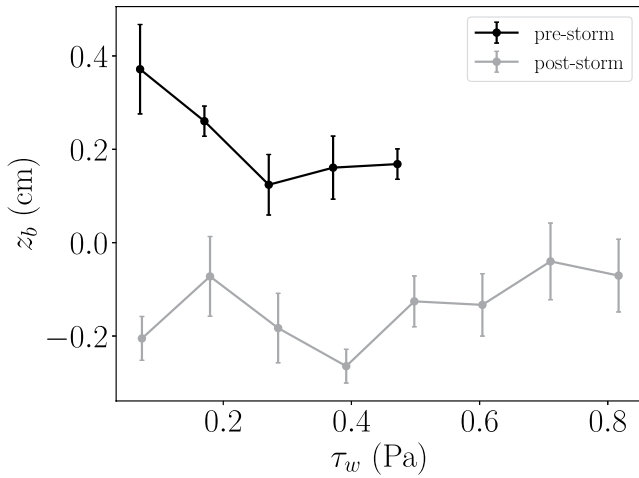


**Figure 6.** The fluctuating bed level,  $z_b$ , bin-averaged by the wave shear stress,  $\tau_w$  (Equation 5b), for the 3 days prior to the 04/20 storm (black line) and 3 days afterward (gray line). Error bars denote the standard error on the bin-averaging.

on average much lower, remaining approximately constant despite the bed being subjected to larger wave shear stresses than in the pre-storm period. This suggests that it had become more difficult to erode the bed, another indication that the exposed bed was made up of more consolidated sediment rather than loose fluff after the storm. This interpretation is consistent with the SPI results presented in Section 3.1, where we hypothesized that a recent scouring event may have led to decreased arPD and prism penetration depth. It is possible that this storm was such an event, and that the unconsolidated fluff layer did not regain its original thickness by the time we conducted the SPI survey 2 weeks later.

Figures 7a and 7b show the near-bed turbulent sediment flux measured by the Vectrino as a function of wave shear stress for the summer and spring deployments, respectively. The fit to the erosion parameterization (Equation 1) is denoted by the black line. The coefficient of determination for this fit was significantly higher than the fit to Equation 1 using  $\tau = \tau_c$  (Equation 5a), which was  $r^2 = 0.01$  for the summer and  $r^2 = 0.04$  for the spring. Using  $\tau = \tau_w$  (Equation 5c) we obtained  $r^2 = 0.30$  and  $r^2 = 0.35$  for summer and spring, respectively. While all of these correlations are significant at the 95% confidence level for the number of data points used in the regression (771), the correlation is obviously much weaker for the current-induced shear stress. This implies that waves are the primary

driver of near-bed sediment fluxes at this shallow study site, with tidally driven turbulence playing a negligible role. This result is consistent with other studies in similar environments (Brand et al., 2010; Friedrichs et al., 2000).

Given that the erosive flux was best predicted by a parameterization that includes the effects of wave shear, one might expect to find a strong wave peak in the  $c'$  power spectrum. Plotted in Figure 8 are power spectra for the Vectrino-measured SSC, averaged over every wavy burst period from the summer deployment. Spectra are shown at integer multiples of the Stokes wave boundary layer thickness,  $\delta_w = \sqrt{2\nu\omega^{-1}}$ , where  $\nu$  is the fluid kinematic viscosity. For the waves at our study site,  $\delta_w \approx 1$  mm. The SSC spectra show a strong wave peak at  $z = \delta_w$ , but this peak decreases substantially by  $z = 4\delta_w$ , and nearly vanishes by  $z = 6\delta_w$ . At this last height, the power spectral density is greatest at lower frequencies and decays at higher frequencies, which is more indicative of a turbulence-dominated process. The spectral slope of the decay, however, scales as approximately  $f^{-1}$ , rather than  $f^{-5/3}$  as theory predicts in the inertial subrange (G. Batchelor et al., 1959; G. K. Batchelor, 1959). An  $f^{-1}$  slope is predicted (and has been measured) in scalar spectra at frequencies above the inertial subrange (e.g., H. Grant et al., 1968), but the spectra in Figure 8 exhibit that slope over a

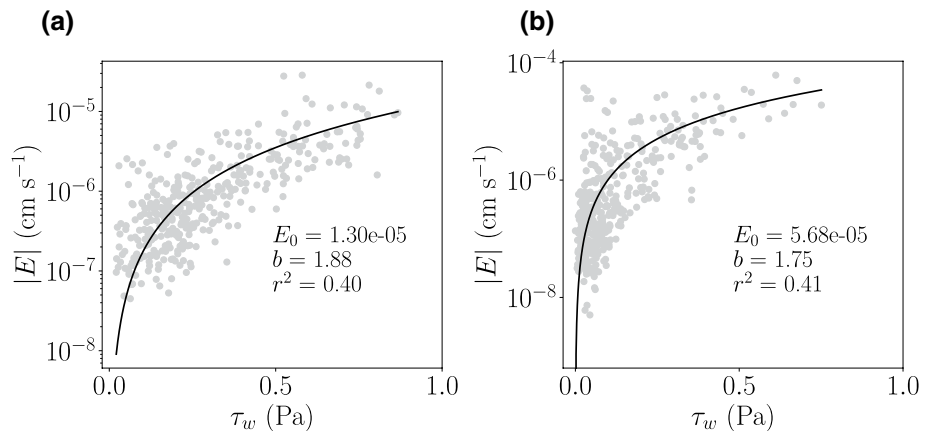


**Figure 7.** The erosive flux magnitude,  $|E|$  (Equation 6) measured by the Vectrino and plotted against the wave shear stress,  $\tau_w$  (Equation 5b), for both the (a) summer and (b) spring deployments. The black line denotes a fit to Equation 1 with associated parameters listed in each panel.

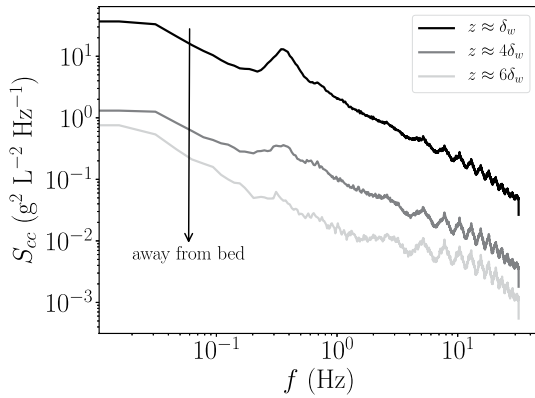


**Figure 8.** The power spectral density of SSC at heights of  $\delta_w$ ,  $4\delta_w$ , and  $6\delta_w$  above the bed. Spectra are averaged over all wavy burst periods from the summer deployment. SSC, suspended sediment concentration.

much wider frequency band. There are numerous reasons that our data might vary from theory, namely that the measurements were taken in stratified, wavy conditions near a boundary, rather than homogeneous isotropic turbulence.

These measurements show that wave-induced sediment resuspension is restricted to the wave boundary layer. Outside that region, waves merely oscillate a constant concentration back and forth along the path of the wave orbital. This can be explained physically as a consequence of settling in a short-period wind wave-dominated environment. The Stokes wave boundary layer thickness is approximately 1 mm for a three-second wave; assuming a floc settling velocity in the range  $w_s = 0.5\text{--}1 \text{ mm s}^{-1}$ , sediment particles that are eroded into the wave boundary layer settle back down into the fluff layer before they are resuspended by the next wave. These results also agree with Direct Numerical Simulations presented in Nelson and Fringer (2018), which showed that by a height of  $6\delta_w$  above the bed in a combined wave-current flow, there was no wave phase variability in the suspended sediment signal.

From a scaling standpoint, the physical arguments presented above state that the vertical structure of the boundary layer suspended sediment profile is determined by a balance between the wave boundary layer thickness and a settling length scale. Defining a settling height  $w_s T$  and letting the wave boundary layer thickness scale as  $\delta \sim u_* / \omega$ , we find

$$\frac{w_s T}{\delta} \sim \frac{w_s / \omega}{u_{*wm} / \omega} = \frac{w_s}{u_{*wm}} \sim \text{Ro}_w, \quad (8)$$

where  $\text{Ro}_w$  is a wave Rouse number. For  $\text{Ro}_w > 1$ , vertical SSC gradients will only be strong near the bed, so wave stresses will not induce wave phase variability in SSC outside the wave boundary layer (e.g., Figure 8). For  $\text{Ro}_w \ll 1$ , sediment may be transported further upward by vertical wave velocities before settling back down to the bed.

Despite the lack of a wave peak in the SSC power spectrum, the turbulent sediment flux outside the wave boundary layer remains highly correlated to the wave shear stress. This is because the wave shear stress can efficiently mobilize sediments within the wave boundary layer, thus allowing tidally driven turbulence to induce turbulent sediment fluxes. In this sense, we can think of waves as a necessary but not sufficient forcing mechanism to transport sediment away from the bed. We can further examine this point by explicitly separating the wave-induced sediment flux from the turbulence-induced sediment flux via the phase method of Bricker and Monismith (2007). This allows for separation of the total vertical sediment flux,  $\overline{c'w}$ , into its turbulence component,  $\overline{c'w'}$ , and its wave component,  $\overline{c\tilde{w}}$ . We can then plot the erosive flux magnitude  $|E|$  as a function of the current shear stress,  $\tau_c$ , separated into cases of high and low wave sediment flux within the wave boundary layer. The result is shown in Figure 9.

With the exception of one measurement bin at the highest  $\tau_c$  during the summer, the erosive flux was significantly larger during burst periods with high  $\overline{c\tilde{w}}$  in the wave boundary layer. During the summer, the average increase in  $|E|$  over the range of  $\tau_c$  was approximately a factor of three; in the spring, the average increase was over an order of magnitude. The seasonal difference could be attributed to the fact that the sediment bed was significantly rougher at P1 during the summer (Figure 4). That roughness could lead to enhanced tidally driven turbulent fluctuations near the bed, which could erode sediment in the absence of a strong wave-driven sediment flux.

A cursory comparison of the relative magnitudes of  $\overline{c'w'}$  and  $\overline{c\tilde{w}}$  belies the significance of the wave-driven sediment flux, which is often smaller than the turbulent sediment flux by two orders of magnitude. This disparity seems counterintuitive given the role of  $\overline{c\tilde{w}}$  in magnifying the turbulent flux (Figure 9), and contrasts with previous studies showing relatively large magnitude wave-driven fluxes over a rippled bed (Smyth et al., 2002). However, it can be explained in the following way: based on the power spectra in Figure 8, it

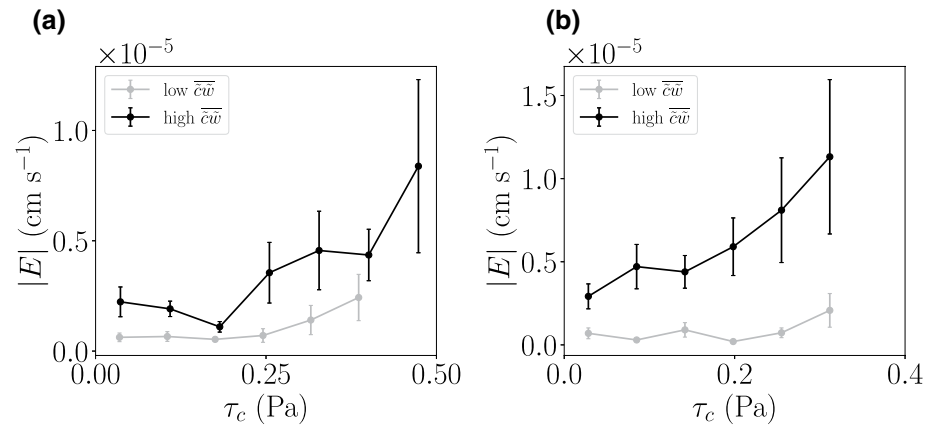


**Figure 9.** The erosive flux,  $|E|$ , plotted as a function of the current shear stress,  $\tau_c$ , for the cases of low  $\overline{c'w'}$  in the wave boundary layer (gray line), and high  $\overline{c'w'}$  in the wave boundary layer (black line) for the (a) summer and (b) spring deployments. High and low  $\overline{c'w'}$  were defined as being, respectively, above and below a 60-h fourth-order Butterworth low-pass filtered  $\overline{c'w'}$  signal.

is clear that waves periodically suspend sediment into the wave boundary layer. Large Eddy Simulations by Chang and Scotti (2006) show that coherent structures set up by interactions between an oscillatory flow and a flat bed can induce this type of upward flux during portions of the wave cycle, and such a mechanism may be responsible for the periodic sediment concentration we see as well. Crucially though,  $\overline{c'w'}$  is not necessarily limited by the amount of sediment supplied by the vertical wave flux. Even if  $\overline{c'w'}$  itself is small, wave stresses can fluidize the bed (Foda et al., 1993), allowing turbulent fluctuations to more readily entrain newly mobilized bed sediments into the overlying flow.

Conceptually, the sediment mobilized within the bed and suspended in the wave boundary layer can be thought of as new, more erodable bed for the tidal currents to erode. This effectively lowers the critical shear stress for erosion, as evidenced by the increasing slope starting near  $\tau_c \approx 0.18$  Pa rather than 0.25 Pa in the summer, and near 0.03 Pa rather than 0.20 Pa in the spring. Similarly, the increased magnitude of  $|E|$  across the range of  $\tau_c$  can be interpreted as an increase in the baseline erosion rate (i.e.,  $E_0$  in Equation 1).

### 3.3. Spatial and Seasonal Variability

The strong correlation between wave strength and erosion was not universal across seasons and study sites. Table 3 lists the fitting parameters for Equation 1 at each 15 cm ADV for all three deployment periods. We have neglected platforms 4a/b from this analysis because they were not deployed in the same location during each of the three seasons. The fits to Equation 1 were carried out using the current-induced, wave-induced, and combined wave current shear stress estimates (Equations 5a–5c). Confidence intervals (at a significance level  $\alpha = 0.05$ ) were calculated for each of the fitting parameters using the bootstrap method, and are listed for each best-fit value of the erodability,  $E_0$ , and the power,  $b$ . For the minimum number of data points used in any of the regressions (379), the Pearson's critical correlation coefficient at the 95% confidence level was  $r^2 = 0.01$ , so even the poorest fits were correlated enough to Equation 1 that a comparison of their fitting parameters was appropriate.

At every instrument platform and for all three seasons,  $\tau_c$  performed the worst in terms of  $r^2$  for the Equation 1 fit. The disparity was especially stark at P1 and P2. At P3, however,  $r^2$  from the current shear stress was often quite close to that derived from the wave-induced and combined wave-current shear stress regressions. Platform 3 was the deepest study site, so it is reasonable to expect the stronger tidal currents to play an outside role in eroding sediment compared to the shallower sites where wave-induced velocities do not decay as much with depth.

Because of variations among the different ADVs' acoustic backscatter to SSC calibrations, it is difficult to compare  $E_0$  values across instruments. The power,  $b$ , however, describes how erosion evolves with shear

**Table 3**  
Fitting Parameters  $E_0$  and  $b$  From 1 for the 15 cmab ADVs at P1, P2, and P3 for the Summer, Winter, and Spring Deployments

	$E_0$ (cm s <sup>-1</sup> Pa <sup>-b</sup> )			$b$ (-)			$r^2$		
	P1	P2	P3	P1	P2	P3	P1	P2	P3
Summer									
$\tau_w$	1.26e-06 ± 2.89e-07	1.05e-05 ± 3.02e-06	3.88e-06 ± 1.25e-06	1.02 ± 0.20	1.86 ± 1.25	1.69 ± 0.25	0.42	0.18	0.49
$\tau_c$	7.64e-07 ± 2.98e-07	8.54e-06 ± 9.07e-06	1.89e-06 ± 1.32e-06	0.32 ± 0.16	0.16 ± 0.37	1.07 ± 0.45	0.09	0.01	0.30
$\tau_{wc}$	8.80e-07 ± 1.49e-07	7.73e-06 ± 2.36e-06	1.41e-06 ± 2.23e-07	1.00 ± 0.19	1.81 ± 1.09	1.74 ± 0.25	0.37	0.16	0.50
Winter									
$\tau_w$	1.23e-05 ± 1.08e-05	3.09e-05 ± 1.13e-05	7.15e-06 ± 1.75e-06	1.17 ± 0.32	1.33 ± 0.39	1.35 ± 0.18	0.71	0.38	0.57
$\tau_c$	1.92e-06 ± 1.25e-06	8.93e-06 ± 8.42e-05	7.60e-06 ± 2.14e-06	0.55 ± 0.24	0.25 ± 1.27	1.72 ± 0.24	0.16	0.01	0.54
$\tau_{wc}$	5.99e-06 ± 1.42e-05	2.42e-05 ± 6.96e-06	3.64e-06 ± 6.61e-07	1.35 ± 0.96	1.50 ± 0.41	1.80 ± 0.28	0.51	0.34	0.67
Spring									
$\tau_w$	1.14e-05 ± 4.92e-06	2.94e-06 ± 2.56e-06	5.26e-06 ± 5.70e-06	1.42 ± 0.24	3.38 ± 0.73	0.92 ± 0.34	0.61	0.62	0.26
$\tau_c$	1.39e-05 ± 4.69e-05	2.48e-05 ± 4.41e-05	3.93e-06 ± 1.62e-06	1.39 ± 0.97	0.48 ± 0.80	0.90 ± 0.18	0.19	0.01	0.25
$\tau_{wc}$	8.75e-06 ± 3.81e-06	2.39e-06 ± 2.04e-06	3.85e-06 ± 2.18e-06	1.93 ± 0.43	3.19 ± 0.75	1.23 ± 0.38	0.62	0.54	0.32

Note. Goodness-of-fit is indicated by the coefficient of determination ( $r^2$ ) for each of the shear stresses ( $\tau_c$ ,  $\tau_w$ ,  $\tau_{wc}$ ) used in the regression.

stress and should be independent of the specific calibration. In the summer and spring,  $b$  was largest at P2, with the spring values substantially larger than any other deployment location during any season. At P1,  $b$  was also relatively elevated in the spring. Interestingly, the spring  $b$  values at P3 were smaller than in the previous two seasons, perhaps indicating a fundamental difference in the erosive response to shear stress between the shallower and deeper study sites.

In general, regressions using  $\tau_w$  and  $\tau_{wc}$  produced similar estimates for  $b$ , with the  $\tau_c$ -based  $b$  estimate often being significantly smaller. The exception to this trend is the winter and spring P3 data, where the current-induced shear stress regression produced  $b$  values within the error bounds of the wave and combined wave-current estimates. Again, this is likely due to the greater water depth at P3, which led to relatively weaker waves and stronger tidal currents.

### 3.4. Nondimensional Analysis

While the results in Table 3 offer insight into the factors controlling erosion at specific times and locations in San Francisco Bay, it is also useful to examine erosion trends as a function of nondimensional numbers that can be applied to other wavy flows. Specific nondimensional parameters that help to quantify the relative importance of waves and tidal currents include the depth-normalized significant wave height,  $H_{sig}h^{-1}$ , the wave-current velocity ratio,  $u_b\bar{u}^{-1}$ , the wave Reynolds number,  $Re_\delta = u_bA_b\nu^{-1}$  (where  $A_b$  is the wave-orbital excursion amplitude), the relative depth,  $kh$ , and the relative roughness,  $k_bA_b^{-1}$ . Each of these parameters was estimated for each 15 cmab ADV measurement burst period at platforms 1, 2, 3, and 4a/4b for all three deployments. We neglected burst periods where  $u_b < 0.04$  m s<sup>-1</sup> because it was difficult to reliably estimate a wave frequency (and thus, wavenumber) from the power spectra during these relatively weak wave periods. This resulted in a total of 4,190 burst periods for analysis.

To quantify the capability of wave and current stresses to predict the turbulent sediment flux, we separated  $\tau_c$ ,  $\tau_w$ , and  $|E|$  into bins sorted by each of the nondimensional parameters listed above. This binning was performed for individual ADVs to mitigate inter-instrument differences in the backscatter-SSC conversion. Equation 1 was fit to the measured  $|E|$  using both  $\tau_c$  and  $\tau_w$ . The resulting  $r^2$  and  $b$  were averaged across the different instruments for each nondimensional parameter bin. We did not analyze  $E_0$  in this procedure because it depends too strongly on the specific acoustic backscatter-SSC calibration.

Out of all of the nondimensional numbers, we found that the wave-current velocity ratio,  $u_b\bar{u}^{-1}$ , and relative depth,  $kh$ , exerted the strongest control on the best-fit parameters, that is, the variance in the erosion

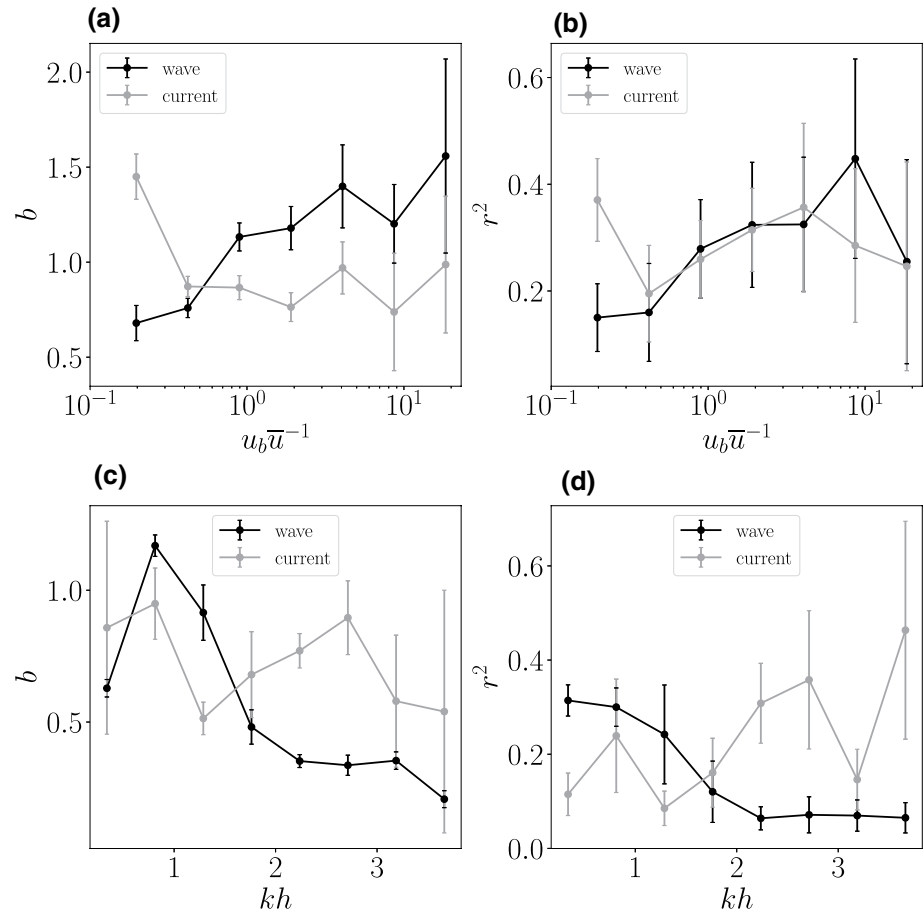


**Figure 10.** (a and c) The power,  $b$ , from a regression of 15 cmab ADV data to Equation 1, using the wave shear stress (black line) and current shear stress (gray line). Data are binned by (a) wave-current velocity ratio,  $u_b \bar{u}^{-1}$ , and (c) relative depth,  $kh$ , for individual instruments, and error bars denote the standard error on the regression, propagated through the average across the instruments. (b and d) The coefficient of determination,  $r^2$ , estimated using the same regression procedure as in panels (a and c).

parameters was highest as a function of the wave-current velocity ratio and relative depth. Figure 10a shows the evolution of the power,  $b$ , with the wave-current velocity ratio. When regressing using the wave shear stress,  $b$  increases steadily as the wave-orbital velocity increases in relation to the mean current velocity. In contrast, when using  $\tau_c$  in the regression,  $b$  decreases before leveling off as the relative contribution of the mean current velocity becomes weaker. This is an intuitive result, indicating that the sediment bed responds more strongly (in terms of erosion) to whichever type of shear stress is dominant at a given time.

Figure 10b shows  $r^2$  for the erosion regressions as a function of  $u_b \bar{u}^{-1}$ . The data are noisier here, but in general  $r^2$  increases with the wave-current velocity ratio when using the wave shear stress. The coefficient of determination is highest for the lowest wave-current velocity ratio bin when using  $\tau_c$ . Notably, that is the only measurement bin where the current-induced shear stress produces a higher  $r^2$  than the wave shear stress. This too is an intuitive result; when the mean current magnitude significantly outweighs the wave-induced velocity magnitude, sediment fluxes will be better correlated to the tidal shear stress.

We next examine erosion trends across relative depth,  $kh$ . Both the power,  $b$  (Figure 10c), and  $r^2$  (Figure 10d) decrease with  $kh$  when using  $\tau_w$  in the regression. This implies that in the shallow water limit, where wave orbitals do not decay with depth, wave shear stresses are more strongly correlated to the turbulent sediment flux. As  $kh$  increases through the intermediate depth range and into the deep water limit at the highest  $kh$  bin, the wave shear stress becomes a poor predictor of erosion. Conversely, the relationship between the current-induced shear stress and the turbulent sediment flux grows stronger with increasing  $kh$ , as indicated by



**Table 4**  
Fitting Parameters Obtained Through Regression of  $I$  to SEDflume Erosion Data

	$E_0$ (cm s <sup>-1</sup> Pa <sup>-b</sup> )	$b$ (-)	$\tau_{cr}$ (Pa)	$r^2$
P1	3.74e-5	1.48	0.18	0.86
P2	6.52e-5	1.76	0.11	0.95
P3	5.02e-5	1.90	0.13	0.83

the increased  $r^2$  (Figure 10d). The relationship with  $b$  is noisier, however, and remains approximately constant within the error bounds.

The results in Table 3 and Figure 10 emphasize that it is critical to take local hydrodynamic conditions into account when parameterizing sediment transport in numerical models. Our data show that both  $u_b \bar{u}^{-1}$  and  $kh$  are particularly useful nondimensional numbers to consider when determining the dominant physical factors that influence erosion at a specific site.

### 3.5. SEDflume and Near-Bed ADV Comparison

One goal of this study was to compare SEDflume erosion measurements with *in situ* sediment flux measurements to assess whether laboratory measurements could adequately represent field conditions. To this end, we can compare the erodability,  $E_0$ , and power,  $b$ , parameters estimated from a regression to Equation 1 for the SEDflume, 5 cmab ADV, and Vectrino data. We also estimated the critical shear stress,  $\tau_{cr}$ , because the estimates are based on near-bed sediment flux measurements (we did not do this for the 15 cmab ADV data in Table 3). For this data set, the comparison between *in situ* velocimeter and SEDflume data comes with an additional caveat: wave shear stresses were primarily responsible for eroding sediment at our measurement sites in the summer. The SEDflume, conversely, applies a steady shear stress to the sediment bed. In each of these cases, we would expect fundamentally different mean shear and turbulence statistics for a given magnitude of mean flow, and thus, different mechanisms for erosion.

Despite these differences, the exponential parameter,  $b$ , estimated from Vectrino and P1 ADV erosion data compared favorably with the P1 SEDflume value when using either the wave or combined wave-current shear stress (Table 4 vs. Table 5), with the  $\tau_{wc}$  estimate from the P1 ADV agreeing best. The critical shear stress values, on the other hand, were significantly larger when calculated using Vectrino and ADV data. The Vectrino and SEDflume showed closer agreement in  $\tau_{cr}$  when using the wave shear stress, though they still differ by at least a factor of 1.5. This is likely because of uncertainty in both the Vectrino backscatter calibration and the SEDflume testing. These confounding factors also affect the  $E_0$  estimates. The Vectrino wave shear stress estimate was closest, perhaps because it was measuring at the sediment bed, but the ADV estimates underpredicted  $E_0$  by an order of magnitude.

At P2, we found poor agreement between the SEDflume and ADV erosion estimates. This is largely due to the noisy P2 ADV data in the summer (note the extremely low  $r^2$  values). The regressions were cleaner in the winter and produced  $\tau_{cr}$  and  $b$  estimates that agreed reasonably well with the SEDflume estimates. Given the high temporal variability of bed characteristics, however, these correlations should be interpreted with caution.

The results at P1 must also be analyzed in terms of temporal variability. One important difference between the SEDflume and velocimeter-derived erosion estimates is that the SEDflume cores were collected at a single point in time, while the Vectrino and ADV regressions were based on multiple weeks of data. This did not significantly affect the summer results; the velocimeters and SEDflume gave very similar erosion rate estimates. And while we do not have SEDflume data for the spring, the temporal variability of erosion rates can be analyzed in terms of the SPI survey data, which showed significantly reduced penetration depth in the spring compared to the winter. This clashes with  $E_0$  and  $b$  estimates from the P1 ADV, which were higher in the spring compared to the winter. The SPI survey, however, occurred after the large storm event depicted in Figure 5, so it observed a less erodable bed. The ADVs and Vectrino, conversely, observed a highly erodable bed before the storm event, which biased the timeseries estimates of erosion parameters. This highlights the time-varying nature of erosion rates and emphasizes the importance of including multilayer beds in sediment transport models.

### 3.6. Comparison to Previous Work

Finally, it is worthwhile to compare our erosion measurements to similar field studies. The most directly comparable are those conducted by Brand et al. (2010), and further analyzed in Brand et al. (2015), where

**Table 5**  
Fitting Parameters to 1 for the Vectrino (*Vec*) and 5 cmab ADVs at Platforms 1 (*P1*) and 2 (*P2*)

	$E_0$ (cm s <sup>-1</sup> Pa <sup>-b</sup> )			$b$ (-)			$\tau_{cr}$ (Pa)			$r^2$		
	Vec	P1	P2	Vec	P1	P2	Vec	P1	P2	Vec	P1	P2
Summer												
$\tau_w$	1.30e-05 ± 5.67e-06	2.96e-06 ± 3.36e-07	1.25e-05 ± 2.71e-06	1.88 ± 0.56	1.62 ± 0.26	0.47 ± 0.44	0.27	0.79	5.86	0.40	0.62	0.03
$\tau_c$	2.86e-06 ± 1.42e-05	1.64e-06 ± 1.03e-06	8.67e-06 ± 3.98e-06	0.19 ± 1.05	0.54 ± 0.30	-0.04 ± 0.26	-	-	0.00	0.01	0.11	0.00
$\tau_{wc}$	6.53e-06 ± 1.76e-06	1.67e-06 ± 1.48e-07	1.13e-05 ± 2.12e-06	1.70 ± 0.50	1.48 ± 0.18	0.44 ± 0.53	0.45	1.40	9.04	0.30	0.54	0.02
Winter												
$\tau_w$	-	2.02e-06 ± 1.89e-06	5.09e-05 ± 5.28e-05	-	0.72 ± 0.34	1.28 ± 1.22	-	-	0.15	-	0.31	0.37
$\tau_c$	-	4.82e-07 ± 4.09e-07	9.12e-06 ± 1.05e-05	-	0.25 ± 0.23	0.12 ± 0.33	-	-	-	-	0.06	0.00
$\tau_{wc}$	-	1.18e-06 ± 2.51e-06	4.18e-05 ± 3.32e-05	-	0.79 ± 0.85	1.52 ± 1.29	-	-	0.16	-	0.21	0.33
Spring												
$\tau_w$	5.68e-05 ± 7.58e-05	6.00e-06 ± 1.00e-06	1.60e-06 ± 3.29e-06	1.75 ± 0.93	1.03 ± 0.11	4.17 ± 1.90	0.12	1.28	0.26	0.41	0.62	0.12
$\tau_c$	1.38e-05 ± 5.51e-05	8.61e-06 ± 8.68e-06	1.25e-05 ± 2.50e-05	0.65 ± 0.83	1.16 ± 0.42	0.13 ± 0.80	1.56	0.71	-	0.04	0.25	0.00
$\tau_{wc}$	3.33e-05 ± 3.76e-05	4.87e-06 ± 7.09e-07	1.58e-06 ± 2.49e-06	2.13 ± 1.47	1.37 ± 0.13	3.64 ± 2.10	0.15	0.79	0.30	0.35	0.64	0.10

Note. The critical shear stress,  $\tau_{cr}$  (Pa), corresponds to 0.5 mm of erosion over 10 min. Estimated critical shear stress values  $\tau_{cr} > 10$  Pa were considered physically unrealistic and were removed from the table.

Equation 1 was fit to ADV turbulent sediment flux measurements using a combined wave-current shear stress during a fall deployment and a spring deployment. Conditions in South San Francisco Bay are quite similar in the fall and summer, so our summer data can be compared to their fall data. In terms of the power,  $b$ , Brand et al. (2015) estimated  $b = 1.33 \pm 0.03$  during the fall, which was close to our summer ADV estimate,  $b = 1.48 \pm 0.18$ , and within the confidence bounds of our Vectrino estimate,  $1.70 \pm 0.50$ . The spring ADV estimates are further from each other ( $b = 2.03 \pm 0.06$  vs.  $b = 1.37 \pm 0.13$ ). The Vectrino estimate was closer, albeit with wider uncertainty bounds ( $2.13 \pm 1.47$ ). In terms of the erodability,  $E_0$ , our values were generally lower than those reported in Brand et al. (2015), though the Vectrino spring  $E_0$  estimate was within the error bounds of their value. Despite the inherent noise in the data, it is encouraging that two sets of field studies conducted eight years apart in the same general sub-basin found comparable erosion rates. This implies that despite the high-frequency variability of hydrodynamic and sediment bed conditions, sediment transport models can achieve reasonable long-term accuracy with prudent choices for bulk erosion parameters.

#### 4. Conclusions

Our analysis showed that waves are often the dominant driver of cohesive sediment erosion in shallow, wave- and current-driven flows. We found that the physical mechanism allowing waves to enhance resuspension is a “wave sediment flux,” analogous to the wave momentum flux, that is only measurable within and directly outside the wave boundary layer. To our knowledge, this is the first *in situ* measurement of the wave sediment flux in an estuarine bottom boundary layer, though previous field studies have hypothesized that sediment entrainment in the wave boundary layer allows for enhanced resuspension by tidal currents (Brand et al., 2010; MacVean & Lacy, 2014). This result also agrees with high resolution numerical simulations (Nelson & Fringer, 2018), and is qualitatively similar to sediment dynamics observed under lower frequency waves in wave-supported mud layers (e.g., Friedrichs et al., 2000; Hsu et al., 2009). Our results also emphasize the importance of using a shear stress that includes the effects of waves when parameterizing erosion in a sediment transport model. This is especially important when the flow is within a lower relative depth regime, or if the wave-orbital velocity significantly exceeds the mean current velocity. In both cases, we found that tidally driven turbulence plays a negligible role in inducing turbulent sediment fluxes.

We also presented *in situ* sediment flux measurements within the wave-current boundary layer, which showed general agreement with erosion measurements taken in a more traditional sediment flume, and

with ADVs placed further from (though still close to) the bed. The trends in our sediment flux measurements, specifically the relatively strong and weak responses to wave forcing before and after a storm-induced erosion event, are consistent with measurements of the relatively unconsolidated fluff layer that we imaged during the SPI survey. These results also emphasize the importance of considering scour history when parameterizing cohesive sediment erosion.

Taken together, the benthic survey, SEDflume data, and boundary layer flux measurements paint a comprehensive picture of an estuarine sediment bed subjected to various degrees of wave and tidal stresses. Given their consistency with SEDflume data, the Vectrino boundary layer measurements show particular promise for characterizing the in situ response to these hydrodynamic forcing mechanisms, especially when coupled with bed level observations. The simultaneous measurement of high resolution wave and turbulence data are particularly valuable for informing erosion parameterizations in cohesive sediment transport models.

### Data Availability Statement

All data used in this paper can be obtained from <https://purl.stanford.edu/wv787xr0534> and <https://purl.stanford.edu/sh883gp0753>.

### Acknowledgments

G. Egan gratefully acknowledges the support of the Charles H. Leavell Graduate Fellowship. This work was funded by the US National Science Foundation under grant OCE-1736668. We thank Frank Spada, Kara Scheu, Craig Jones, Marianne Cowherd, Stephen LaMothe, and Jim Christmann for their assistance with the field work. We also thank Chris Sherwood and the two anonymous reviewers whose comments improved the quality of the manuscript.

### References

- Batchelor, G. K. (1959). Small-scale variation of convected quantities like temperature in turbulent fluid part 1. general discussion and the case of small conductivity. *Journal of Fluid Mechanics*, 5(1), 113–133.
- Batchelor, G., Howells, I., & Townsend, A. (1959). Small-scale variation of convected quantities like temperature in turbulent fluid part 2. the case of large conductivity. *Journal of Fluid Mechanics*, 5(1), 134–139.
- Brand, A., Lacy, J., Gladding, S., Holleman, R., & Stacey, M. (2015). Model-based interpretation of sediment concentration and vertical flux measurements in a shallow estuarine environment. *Limnology and Oceanography*, 60(2), 463–481.
- Brand, A., Lacy, J., Hsu, K., Hoover, D., Gladding, S., & Stacey, M. (2010). Wind-enhanced resuspension in the shallow waters of south san francisco bay: mechanisms and potential implications for cohesive sediment transport. *Journal of Geophysical Research: Oceans*, 115(C11), C11024. <https://doi.org/10.1029/2010JC006172>
- Brennan, M. L., Schoellhamer, D. H., Burau, J. R., & Monismith, S. G. (2002). *Tidal asymmetry and variability of bed shear stress and sediment bed flux at a site in San Francisco Bay, USA*. In Proceedings in marine science (5, pp. 93–107) Elsevier.
- Bricker, J. D., & Monismith, S. G. (2007). Spectral wave–turbulence decomposition. *Journal of Atmospheric and Oceanic Technology*, 24(8), 1479–1487.
- Cartwright, G. M., Friedrichs, C. T., & Smith, S. J. (2013). A test of the adv-based Reynolds flux method for in situ estimation of sediment settling velocity in a muddy estuary. *Geo-Marine Letters*, 33(6), 477–484.
- Chang, Y. S., & Scotti, A. (2006). Turbulent convection of suspended sediments due to flow reversal. *Journal of Geophysical Research: Oceans*, 111(C7), C07001. <https://doi.org/10.1029/2005JC003240>
- Christoffersen, J. B., & Jonsson, I. G. (1985). Bed friction and dissipation in a combined current and wave motion. *Ocean Engineering*, 12(5), 387–423.
- Coffey, F. C., & Nielsen, P. (1987). The influence of waves on current profiles. In *Coastal engineering 1986* (pp. 82–96).
- Egan, G., Chang, G., Revelas, G., Monismith, S., & Fringer, O. (2020). Bottom drag varies seasonally with biological roughness. *Geophysical Research Letters*, 47(15), e2020GL088425.
- Egan, G., Cowherd, M., Fringer, O., & Monismith, S. (2019). Observations of near-bed shear stress in a shallow, wave-and current-driven flow. *Journal of Geophysical Research: Oceans*, 124(8), 6323–6344.
- Egan, G., Manning, A. J., Chang, G., Fringer, O., & Monismith, S. (2020). Sediment-induced stratification in an estuarine bottom boundary layer. *Journal of Geophysical Research: Oceans*, 125(8), e2019JC016022.
- Foda, M. A., Hunt, J. R., & Chou, H.-T. (1993). A nonlinear model for the fluidization of marine mud by waves. *Journal of Geophysical Research: Oceans*, 98(C4), 7039–7047.
- Friedrichs, C., Wright, L., Hepworth, D., & Kim, S. (2000). Bottom-boundary-layer processes associated with fine sediment accumulation in coastal seas and bays. *Continental Shelf Research*, 20(7), 807–841.
- Grant, H., Hughes, B., Vogel, W., & Moilliet, A. (1968). The spectrum of temperature fluctuations in turbulent flow. *Journal of Fluid Mechanics*, 34(3), 423–442.
- Grant, W., & Madsen, O. (1979). Combined wave and current interaction with a rough bottom. *Journal of Geophysical Research: Oceans*, 84(C4), 1797–1808.
- Herbers, T., Elgar, S., & Guza, R. (1999). Directional spreading of waves in the nearshore. *Journal of Geophysical Research: Oceans*, 104(C4), 7683–7693.
- Hsu, T.-J., Ozdemir, C. E., & Traykovski, P. A. (2009). High-resolution numerical modeling of wave-supported gravity-driven mudflows. *Journal of Geophysical Research: Oceans*, 114(C5), C05014. <https://doi.org/10.1029/2008JC005006>
- Lick, W. (1982). The transport of contaminants in the great lakes. *Annual Review of Earth and Planetary Sciences*, 10(1), 327–353.
- Lohrmann, A. (2001). Monitoring sediment concentration with acoustic backscattering instruments. *Nortek Technical Note*, 1, 1–5.
- Maa, J. P., Sanford, L., & Halka, J. P. (1998). Sediment resuspension characteristics in Baltimore Harbor, Maryland. *Marine Geology*, 146(1), 137–145.
- MacVean, L. J., & Lacy, J. (2014). Interactions between waves, sediment, and turbulence on a shallow estuarine mudflat. *Journal of Geophysical Research: Oceans*, 119(3), 1534–1553.
- McNeil, J., Taylor, C., & Lick, W. (1996). Measurements of erosion of undisturbed bottom sediments with depth. *Journal of Hydraulic Engineering*, 122(6), 316–324.

- Mehta, A. J., & Partheniades, E. (1982). Resuspension of deposited cohesive sediment beds. *Coastal Engineering*, 1982, 1569–1588.
- Mei, C. C., Fan, S.-j., & Jin, K.-r. (1997). Resuspension and transport of fine sediments by waves. *Journal of Geophysical Research: Oceans*, 102(C7), 15807–15821.
- Merritt, W. S., Letcher, R. A., & Jakeman, A. J. (2003). A review of erosion and sediment transport models. *Environmental Modelling & Software*, 18(8–9), 761–799.
- Nelson, K., & Fringer, O. (2018). Sediment dynamics in wind wave-dominated shallow-water environments. *Journal of Geophysical Research: Oceans*, 123(10), 6996–7015.
- Papanicolaou, A. T. N., Elhakeem, M., Krallis, G., Prakash, S., & Edinger, J. (2008). Sediment transport modeling review—current and future developments. *Journal of Hydraulic Engineering*, 134(1), 1–14.
- Revelas, E., Sackmann, B., Thurlow, A., Jones, C. (2018). Mapping benthic habitat conditions and seafloor deposits using sediment profile imaging and a semiautomated image processing system. In *Offshore technology conference*.
- Rhoads, D. C., & Germano, J. D. (1982). Characterization of organism-sediment relations using sediment profile imaging: An efficient method of remote ecological monitoring of the seafloor (remots super (tm) system). *Marine ecology progress series. Oldendorf*, 8(2), 115–128.
- Rhoads, D. C., & Germano, J. D. (1987). Interpreting long-term changes in benthic community structure: a new protocol. In *Long-term changes in coastal benthic communities* (pp. 291–308) Springer.
- Roberts, J., Jepsen, R., Gotthard, D., & Lick, W. (1998). Effects of particle size and bulk density on erosion of quartz particles. *Journal of Hydraulic Engineering*, 124(12), 1261–1267.
- Sanford, L. P. (2008). Modeling a dynamically varying mixed sediment bed with erosion, deposition, bioturbation, consolidation, and armoring. *Computers & Geosciences*, 34(10), 1263–1283.
- Sanford, L. P., & Halka, J. P. (1993). Assessing the paradigm of mutually exclusive erosion and deposition of mud, with examples from upper chesapeake bay. *Marine Geology*, 114(1–2), 37–57.
- Sanford, L. P., & Maa, J. P. (2001). A unified erosion formulation for fine sediments. *Marine Geology*, 179(1), 9–23.
- Smyth, C., Hay, A. E., & Zedel, L. (2002). Coherent doppler profiler measurements of near-bed suspended sediment fluxes and the influence of bed forms. *Journal of Geophysical Research: Oceans*, 107(C8), 19–1.
- Van Maren, D., van Kessel, T., Cronin, K., & Sittoni, L. (2015). The impact of channel deepening and dredging on estuarine sediment concentration. *Continental Shelf Research*, 95, 1–14.
- Welch, P. (1967). The use of fast fourier transform for the estimation of power spectra: A method based on time averaging over short, modified periodograms. *IEEE Transactions on Audio and Electroacoustics*, 15(2), 70–73. <https://doi.org/10.1109/TAU.1967.1161901>
- Wiberg, P. L., & Sherwood, C. R. (2008). Calculating wave-generated bottom orbital velocities from surface-wave parameters. *Computers & Geosciences*, 34(10), 1243–1262.
- Winterwerp, J. C., & Van Kesteren, W. G. (2004). *Introduction to the Physics of Cohesive Sediment Dynamics in the Marine Environment*, Developments in Sedimentology. 56, Elsevier.
- Wood, P. J., & Armitage, P. D. (1997). Biological effects of fine sediment in the lotic environment. *Environmental Management*, 21(2), 203–217.
- You, Z.-J., Wilkinson, D., & Nielsen, P. (1991). Velocity distributions of waves and currents in the combined flow. *Coastal Engineering*, 15(5–6), 525–543.